International Journal of Impact Engineering 180 (2023) 104714

Contents lists available at ScienceDirect

International Journal of Impact Engineering

journal homepage: www.elsevier.com/locate/ijimpeng

Insights into protective performance of CoCrNi medium entropy alloy coating subjected to supersonic micro-ballistic impact

J.L. Dong [a], F.C. Li [c], X.Q. Wu [b,*], G.J. Wang [a,*], X.P. Zhang [a], B.Q. Luo [a], X.M. Chen [a], F.L. Tan [a], Y.H. Liu [c], M.Q. Jiang [b,e], J.H. Zhao [d], C.G. Huang [e], C.W. Sun [a]

[a] Institute of Fluid Physics, China Academy of Engineering Physics, Mianyang, 621999, China
[b] Institute of Mechanics, Chinese Academy of Sciences, 100190, Beijing, China
[c] Institute of Physics, Chinese Academy of Sciences, 100190, Beijing, China
[d] Institute of Applied Electronics, China Academy of Engineering Physics, Mianyang, 621999, China
[e] School of Engineering Science, University of Chinese Academy of Sciences, Beijing 100049, China

ARTICLE INFO

Keywords:
Medium entropy alloy
Protective coating
Supersonic microparticle impact
Impact-mode ratio
Protective performance

ABSTRACT

Medium- and high-entropy alloys (MEAs and HEAs) coatings have attracted increasing attention owing to their exceptional mechanical properties and potential applications in structures protective from supersonic microparticle impact. However, there are no experimental insights into their protective performance. In this study, we fabricated high-quality amorphous CoCrNi MEA coatings with a thickness of 4.5 μm on the rigid and flexible substrates through ion beam-assisted deposition. Based on nanoindentation and laser-induced supersonic microparticle impact experiments, the mechanical properties and protective performance of the CoCrNi MEA coating were characterized and compared with those of the aluminum and copper coating. The results show that the CoCrNi MEA coating exhibits a high hardness of 9.7 GPa and an elastic modulus of 146.8 GPa. Under the supersonic impact, the CoCrNi MEA coating shows high coefficient of restitution, low rebound-to-fracture transition velocity, and small impact-mode ratios. The impact-mode ratios of the CoCrNi MEA coating subjected to microparticles of different materials further indicate that the CoCrNi MEA coating can efficiently withstand the high-velocity impact of most metallic particles except tungsten ones. Our work provides direct experimental insights into the excellent impact resistance of CoCrNi MEA coatings, which holds a great promise for improving the reliability and durability of equipment subjected to high-speed collisions of solid particles entrained within the air such as ice and sand dust.

1. Introduction

As advanced materials, medium- and high-entropy alloys (MEAs and HEAs) have attracted considerable interest due to their superior properties [1–5], such as exceptional fracture toughness [6–8], outstanding strength-ductility synergy [9–12], and superior "self-sharpening" capability [13]. These good mechanical properties enable MEAs and HEAs to exhibit remarkable potential applications as structural materials in extreme service environments [14–16].

MEAs/HEAs have been developed as advanced coating materials over the past few years. For instance, amorphous TiNbZrMoV and AlCrFeMoTi HEA coatings provide excellent corrosion resistance owing to the low intrinsic solubility of the coating composition elements and the limitation of element out-diffusion or segregation from the steel and coating [17,18]. The addition of Nb to the $Fe_{0.25}Co_{0.25}Ni_{0.25}(B_{0.7}Si_{0.3})_{0.25}$ HEA coating dramatically improves the wear resistance owing to the formation of an amorphous structure with high elastic modulus [19]. The CoCrNi MEA coating exhibits enhanced hardness and damage tolerance due to its nanotwinned structure upon micro-indentation system [20].

The high-performance MEAs/HEAs coatings are also regarded as promising protective materials that effectively protect the equipment from extreme impact loads and improve reliability and durability during service. For instance, it could improve the surface integrity of jet engine turbine blades subjected to high-speed collisions of solid particles entrained within the air, such as ice, hailstones, and sand dust [21,22]. Recent studies have reported that bulk HEAs exhibit excellent ballistic performance and can provide effective anti-ballistic impact capabilities

* Corresponding authors.
E-mail addresses: wuxianqian@imech.ac.cn (X.Q. Wu), wangguiji@126.com (G.J. Wang).

https://doi.org/10.1016/j.ijimpeng.2023.104714
Received 30 March 2023; Received in revised form 12 June 2023; Accepted 25 June 2023
Available online 28 June 2023

[23–25]. This is dominantly beneficial from its active dislocations and nanotwins generated at high strain rates. High dislocation and nanotwin densities make the HEA easier to strain hardened with elevated toughness to resist high-speed deformation. As the size decreases, metallic samples with characteristic sizes of several micrometers have exhibited a remarkable size effect, that is, the smaller the stronger [26–28]. The MEAs/HEAs coatings with micron thicknesses are also expected to possess excellent impact resistance due to their possible size effect subjected to the impact of microparticles. However, there is no direct experimental proof to date.

In this study, a novel amorphous CoCrNi MEA coating was deposited on silicon (Si) and polycarbonate (PC) substrates. We carried out high-velocity microparticle impact on the CoCrNi MEA coating to obtain its protective performance. Post-impact observations and the coefficient of restitution were examined to determine the impact resistance of the CoCrNi MEA coating. The comparison of impact-mode ratios indicates that the CoCrNi MEA coating can effectively withstand the high-velocity impact of most metallic particles, providing solid evidence of the CoCrNi MEA coating with extraordinary protective performance against microparticle impact.

2. Materials and methods

2.1. Deposition and characterization of CoCrNi coating

A CoCrNi MEA was chosen as the model material because its bulk sample shows high strength (~1.5 GPa) and considerable tensile plasticity (~60%) [29,30]. Among the equiatomic subsystems of CrMnFeCoNi, the CrCoNi MEA exhibited the best combination of strength and ductility. The CoCrNi deposition target was obtained by arc-melting Co, Cr, and Ni mixtures with 99.99% purity in a high-purity argon atmosphere. Ion beam-assisted deposition (IBAD) was used to deposit CoCrNi coatings on Si (rigid) and PC (flexible) substrates with a thickness of 1 mm. The ion beam current was 10 mA, and the beam energy was 750 eV during the deposition process. The depositing argon pressure was 2.4×10^{-2} Pa, and the deposition time was 4 h. The hardness and modulus of the CoCrNi coating were investigated using a nanoindentation tester (Agilent, Nano Indenter G200) with a load precision of 50 nN in the continuous stiffness mode. The holding time was fixed to be 5 s. Field-emission scanning electron microscopy (SEM, JEOL S4800) with energy dispersive X-ray spectrometry (EDS), carried out at an accelerating voltage of 20 kV, was utilized to perform post-impact observations. The phases of the coating were detected using X-ray diffraction (XRD) through Cu-Kα radiation at a rate of 0.02°/s in the 2θ range of 20° to 90° The impact-induced craters were measured using a profilometer (Dektak X, Bruker).

2.2. Laser-induced microparticle high-velocity impact

To explore the impact resistance performance of the CoCrNi MEA coatings, we built the laser-induced micro-projectile impact test (LIPIT) platform. It opens a window for directly studying the mechanical response and deformation behavior of materials under extreme dynamic conditions [31,32]. The impact target was placed ~1.5 mm away from the projectile launch pad, and a K9 glass substrate was coated first with a 100 nm gold layer (laser ablation layer), followed by a 40-μm-thick cross-linked polydimethylsiloxane (PDMS) layer (elastic layer). A single laser pulse excited by a Q-switched Nd: YAG laser with a duration of 10 ns and a wavelength of 532 nm was focused into a spot size of 500 μm on the gold film. We selected SiO_2 particles with a diameter (D) of 10–13 μm as projectiles because they have relatively high strength and hardness and cannot easily deform and fracture during impact. A molecular sieve with different screening sizes was used for particle screening before the impact test to ensure almost the same diameter of the microparticles.

Monodisperse SiO_2 micro-projectile was drop-cast and air-dried on the launch pad. Individual projectiles were selectively launched by the rapid expansion of PDMS film via laser-ablation-induced gold vaporization. A range of particle impact velocity from 200 to 1000 m/s was achieved by adjusting the pulse laser energy (40–80 mJ). The impact events were captured in real-time using a high-speed Kirana camera (Specialized Imaging, 5000,000 frames per second, UK) with a NAVISTAR microscope objective lens (12 × magnification, focal length 34 cm), allowing for relatively accurate measurement of the microparticle velocity during impact. An SI-LUX 640 laser (wavelength 640 nm, pulse duration 100 ns) was used for illumination during impact. The interframe time was adjusted from 200 to 500 ns, and the corresponding exposure time was varied from 100 to 200 ns. The impact and rebound velocities of the projectile were calculated by dividing the distance measured between adjacent projectile snapshots in the multi-exposure image by the time interval between consecutive imaging laser pulses.

3. Results and discussion

3.1. Microstructure of deposited CoCrNi MEA coating

Figs. 1(a) and (b) show that the CoCrNi MEA coatings are deposited on rigid Si and flexible PC substrates, respectively. The CoCrNi coating has a smooth surface and can be bent into a roll on a PC substrate, as shown in Fig. 1(b), suggesting that the CoCrNi coating has high flexibility and stability. The EDS mapping with SEM image is displayed in Fig. 1(c), and the Co, Cr, and Ni elements are distributed uniformly in the coating. The XRD profile shows that there is no observable crystalline peak. Only one broad peak corresponding to the amorphous structure is shown in Fig. 1(d). Theoretically, film deposition can be considered an extremely rapid quenching process due to the ultrahigh cooling rates of approximately 10^{14} K/s, in which the deposition atoms have insufficient kinetics to form preferred crystalline structures [18, 33-35]. In addition, the severe lattice distortion caused by the incorporation of atoms of varying sizes leads to topological instability and decreases the driving force for the transformation from an amorphous to a crystalline configuration [5]. Meanwhile, the sluggish diffusion effect, originating from the difficulty of the cooperative diffusion of different atoms, can slow the crystallization kinetics. Considering all the factors mentioned above, an amorphized structure was observed for the CoCrNi MEA coatings. Fig. 1(e) shows clearly that the thickness of CoCrNi coating is 4.5 ± 0.3 μm, and it is tightly deposited on the Si substrate. The CoCrNi coating has a homogeneous structure, and no visible cracks or pores exist between the coating and substrate. The cases mentioned above confirm the successful preparation of an amorphous CoCrNi MEA coating.

3.2. Hardness and elastic modulus of the CoCrNi MEA coating

Our nanoindentation tests effectively evaluate the mechanical properties of the CoCrNi MEA coating. As traditional protective materials, Al and Cu have been widely used in protective structures. Thus, we also deposited ultrafine-grained Al and Cu coatings with the same thickness of approximately 4.5 μm on Si and PC substrates and conducted nanoindentation tests for comparison. As shown in Figs. 2(a) and (b), the distance between the two sites is 10 μm to prevent the reciprocal influence of the indentation sites. We carried out nanoindentation tests with 10 indentations to ensure the adequate accuracy of the measurements and the uniformity of the structure. Fig. 2(c) shows the load-displacement curves of the CoCrNi, the Al, and the Cu coatings. The maximum depth is 390 nm, and the minimum depth is 380 nm. The indentation depth is less than one-tenth of the coating thickness to eliminate the substrate effect. The Al coating exhibits an elastic modulus and hardness of 83.2 ± 3.3 GPa and 3.1 ± 0.4 GPa, respectively, while the Cu coating displays an elastic modulus and hardness of 103.6 ± 3.6 GPa and 4.4 ± 0.6 GPa, respectively. Compared with the Al and Cu coatings, the CoCrNi coating shows the highest elastic modulus and

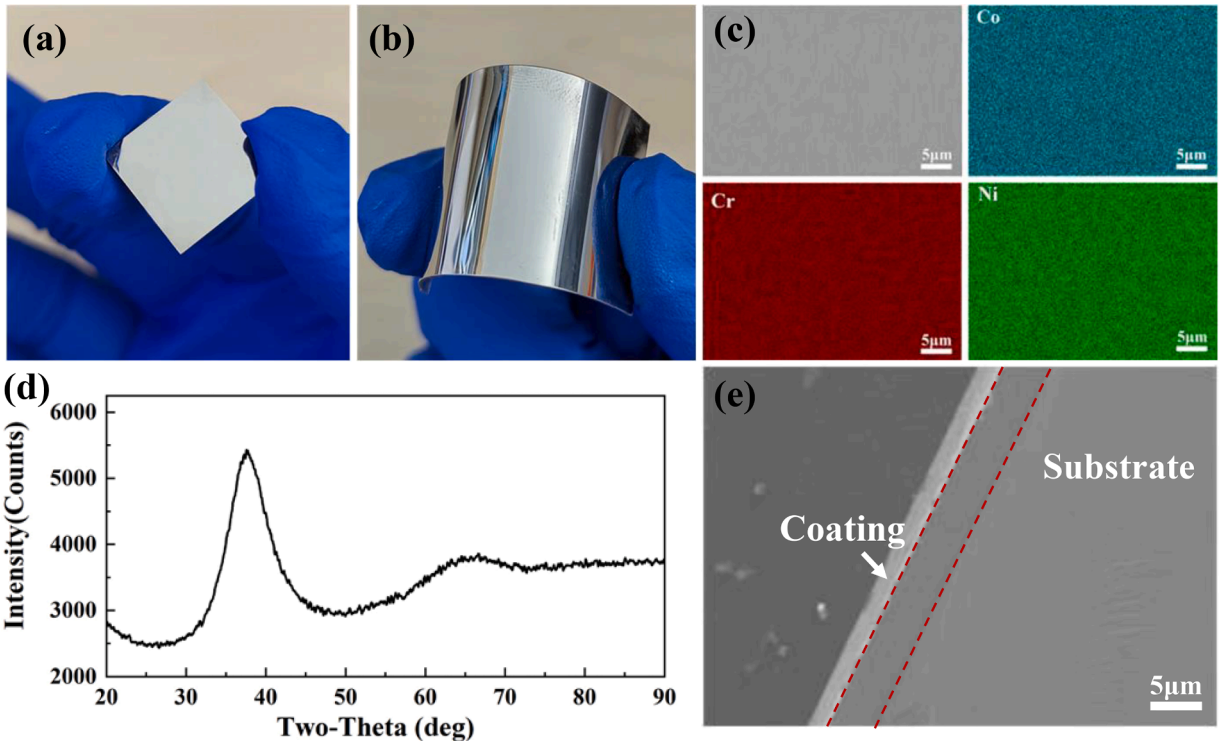

Fig. 1. CoCrNi coatings deposited on (a) Si substrate and (b) PC substrate. (c) EDS mapping of the CoCrNi coating. (d) XRD profile of the CoCrNi coating. (e) Interface between the Si substrate and the CoCrNi coating.

hardness of 146.8 ± 5.0 GPa and 9.7 ± 0.7 GPa, respectively [Figs. 2(d) and (e)]. The superior hardness of the CoCrNi coating is advantageous for enhancing its impact resistance. A comparison of the hardness of the CoCrNi coating and other advanced coatings is presented in Fig. 2(f), including nanotwinned structure CoCrNi MEA coating [20], CoCrFeMnNi HEA coating [36], AlCoCrFeNi HEA coating [37], amorphous AlCrFeMoTi [17] and TiNbZrMoV [18] HEA coatings. The CoCrNi coating exhibits relatively high hardness compared to most other coatings. In addition, the CoCrNi coating possesses the advantage of expedient large-scale fabrication, making it a priority in industrial applications.

3.3. Microparticle impact response of the CoCrNi MEA coating

Fig. 3(a) illustrates the LIPIT platform used in this experiment. The LIPIT technique was originally developed by Lee et al. [38] and was further improved by Veysset and Hassani-Gangaraj et al. [39]. SiO_2 microparticles were used as projectiles in the present experiment, as shown in Fig. 3(b). Figs. 3(c) and (d) show two exemplar snapshots of the impact event where two spherical SiO_2 particles traverse downward from the top of the view field and impact the CoCrNi coating with Si substrate at V_i of 385 m/s [Fig. 3(c)] and 615 m/s [Fig. 3(d)]. Fig. 3(c) clearly shows that the particle rebounds at a velocity of 158 m/s. We did not observe an indication of deformation in the rebounding SiO_2 particles, such as significant deviation from sphericity in our real-time observations or fracture, melting, or erosion of the target in our SEM micrographs. Therefore, the plastic deformation of the target is the dominant operative mechanism that dissipates the energy of incoming particles. A series of fracture regimes occurred when exceeding the yield stress of the particles with increasing V_i. The SiO_2 particle is fractured under an V_i of 615 m/s, as shown in Fig. 3(d).

The high-velocity impacts of micrometer-scale spherical projectiles normal to the coatings surface result in high-strain-rate deformation of the coating material and the formation of impact craters. Figs. 4(a–l) show the post-impact observations of the CoCrNi, the Al, and the Cu coatings with rigid and flexible substrates at V_i of 550 and 730 m/s, respectively. The post-impact morphologies of the impact site show that the CoCrNi, the Al, and the Cu coatings have been deformed plastically but not melted and re-solidified. The CoCrNi coating dissipated the energy of the incoming particles through multiple shear bands, as shown in Figs. 4(a) and (b). Such plastic dissipation is unique to amorphous solids because shear transformations (STs), the basic flow events in amorphous solids, can occur at the nanoscale [40]. These observed shear bands resulted from the localized self-organization of STs under high strain rate loading [41]. The Al coatings dissipate impact energy through severe plastic deformation.

The variations in the deformation area and crater depth as a function of V_i are shown in Figs. 4(m) and (n), respectively. With increasing V_i, the deformation areas of the CoCrNi, the Al, and the Cu coatings increase, suggesting an impact velocity-dependent dynamic behavior. Moreover, for all V_i, the deformation area of the Al and the Cu coatings is larger than that of the CoCrNi coating, indicating that the Al and the Cu coatings are more severely damaged under the microparticle impact [Fig. 4(m)]. Fig. 4(n) shows the variation in the impact-induced crater depth of the CoCrNi, the Al, and the Cu coatings on various substrates. The crater depths of the Al and the Cu coatings are significantly deeper than that of the CoCrNi coating. Moreover, the substrate effect is evident for the Al and the Cu coatings, implying that the flexible substrate suffers a certain degree of plastic deformation. That is, the Al and the Cu coatings did not effectively protect the substrate material. However, for the CoCrNi coating, the impact-induced crater depth remained relatively stable on different substrates and was far lower than the coating thickness. Hence, the CoCrNi coating effectively protected the rigid and flexible substrates during microparticle impact.

3.4. Coefficient of restitution and impact-mode ratio

To further investigate the impact response of the CoCrNi coating, we measured the V_i and rebound velocities (V_r) for each impact and calculated the coefficient of restitution (COR, V_r/V_i) [39]. Fig. 5 shows

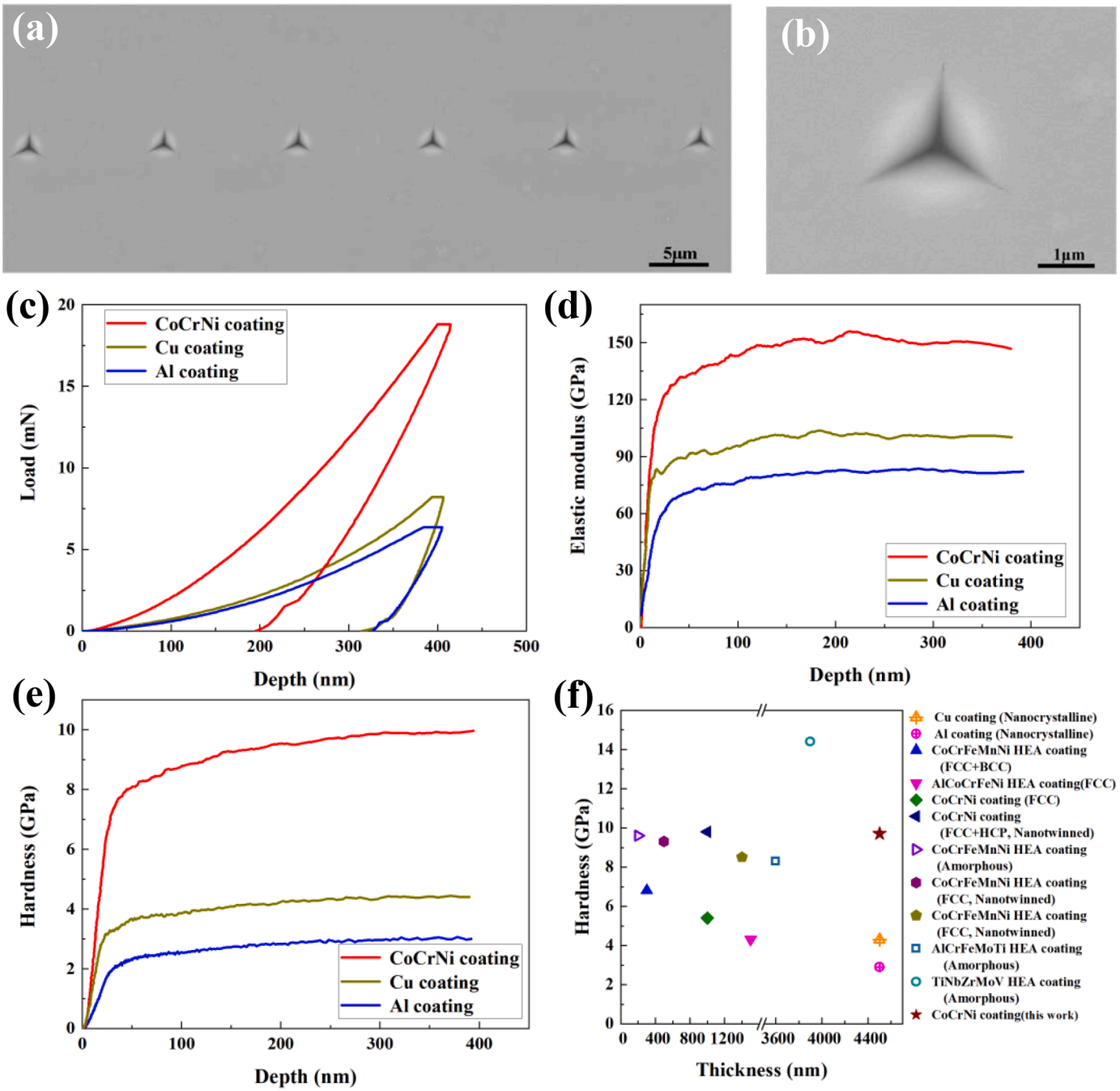

Fig. 2. (a) Spacing between indentation sites. (b) Size of indentation site. (c) Load-displacement curves of the CoCrNi, the Al, and the Cu coatings. (d) Elastic modulus and (e) hardness as functions of the depth of the CoCrNi, the Al, and the Cu coatings. (f) Hardness of the CoCiNi coating in the present study and other coatings as a function of thickness.

COR as a function of V_i for the CoCrNi, the Al, and the Cu coatings deposited on different substrates. The COR shows a linear decline due to the increase of the fraction of energy dissipated through plastic deformation of the target with increasing V_i [39]. The CoCrNi coating exhibits higher COR than the Al and the Cu coatings, indicating that the kinetic energy of the microparticles is less dissipated through the plastic deformation of the CoCrNi coating. Furthermore, the COR of the CoCrNi coatings on the flexible and rigid substrates were almost identical, suggesting that the energy dissipation of the target was mainly contributed by the CoCrNi coatings rather than the substrate. However, the COR of the Al and the Cu coatings deposited on the flexible substrate is significantly lower than that deposited on the rigid substrate, manifesting that the flexible substrate deforms largely and dissipates considerably the impact energy.

The zero COR value indicates the critical velocity (V_{cr}) for the rebound-to-fracture transition of impact modes. Above V_{cr}, the microparticles are yield and ultimate fracture. The V_{cr} of the CoCrNi coatings deposited on rigid and flexible substrates were 543 m/s and 570 m/s, respectively. The varying V_{cr} of the CoCrNi coating on the various substrates suggest that only a small amount of the microparticle energy is absorbed by the flexible substrate. The V_{cr} of the Al coating deposited on the rigid and flexible substrates was 765 m/s and above 850 m/s and Cu coating was 680 m/s and 745 m/s, respectively, showing the significant influence of the substrates. The relatively low V_{cr} of the CoCrNi coating further proves its higher microparticle impact resistance compared to the Al and Cu coatings.

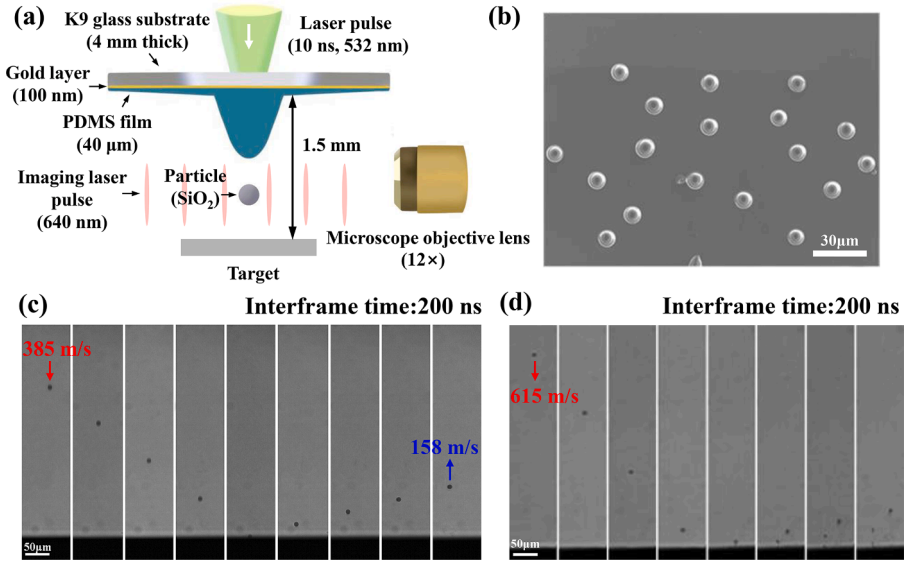

Fig. 3. (a) Schematic of the LIPIT platform. (b) SEM image of SiO_2 microparticles used as projectiles. (c-d) Multiframe sequences with an interframe time of 200 ns and exposure time of 100 ns show that SiO_2 particle impacts a CoCrNi coating with a rigid substrate at 385 and 615 m/s, respectively.

The impact-mode ratio (φ), as proposed by Hassani *et al.* [42], was introduced to quantify the splatting or penetration modes of the impact events,

$$\varphi = \frac{\rho_p C_p^2 Y_p}{\rho_t C_t^2 Y_t}, \tag{1}$$

where ρ, C, and Y are density, sound velocity, and dynamic yield strength, respectively. The subscripts p and t refer to the particle and the target, respectively. Significant fracturing and splatting of the particles occur for $\varphi << 1$. As the φ increases, the deformation in the particle decreases, and the plastic deformation in the target increases. Ideal co-deformation is characterized by $\varphi \approx 1$. For $\varphi >> 1$, the impact-induced plasticity is accommodated predominantly by the target, and deep penetration of particles into the target occurs. It is to be noted that although the impact phenomena in the present study is much more complicated, Eq. (1) can still well predict the deformation modes of the microparticles during impact on various targets, as validated by Hassani *et al.* [42]

The microscale dynamic yield strengths (Y) of materials can be extracted from the V_i and V_r of microparticle impact experiments using an elastic-perfectly plastic (EPP) impact behavior model developed by Wu et al. [43].,

$$Y = \left(\frac{\rho_t E_*^2 V_r^4}{26 V_i^2 \alpha^4}\right)^{1/3}, \tag{2}$$

where E_* is the representative elastic modulus defined by elastic modulus E and Poisson's ratios ν of the two materials,

$$\frac{1}{E_*} = \frac{1-\nu_p^2}{E_p} + \frac{1-\nu_t^2}{E_t}, \tag{3}$$

where E_p and ν_p are elastic modulus and Poisson's ratio for the particle, and E_t and ν_t are elastic modulus and Poisson's ratio for the target material. The α is a factor and determined by the elastic-plastic behavior of the particle and the target material in the impact system. According to the study by Wu et al. [43], $\alpha = 0.62$ for an EPP sphere impacting an elastic substrate and $\alpha = 0.78$ for an elastic sphere impacting an EPP substrate. For the same materials, $\alpha = 0.57$ [44]. Recently, Sun et al. [44] further performed the micro-particle impact tests by Al_2O_3 micro-particle impacting Cu substrate using LIPIT. Their results agree with the EPP impact behavior model, validating the applicability of LIPIT for measuring Y of materials. In the present study, when the SiO_2 microparticles impacts the CoCrNi, the Al, and the Cu coatings, the SiO_2 microparticles can be regarded as elastic spheres and the coatings can be treated as EPP substrates. Consequently, the value of α is taken as 0.78. According to Eq. (2), we can extract the microscale Y of the CoCrNi, the Al, and the Cu coatings by microparticle impact experiments, as shown in Fig. 6 (a-f). The Y of the CoCrNi coatings are determined to be 2380 ±260 MPa for both the rigid and the flexible substrates because the V_r of the CoCrNi coatings for different substrates are almost the same. However, the Y of the Al coating are 439±65 MPa and 253±40 MPa for the rigid and the flexible substrates, respectively, due to the significant difference in V_r for different substrates. The Y of the Cu coating are 696 ±75 MPa and 451±60 MPa for the rigid and flexible substrates, respectively. In order to obtain the Y of SiO_2 so that we can calculate the φ in Eq (1), we performed LIPIT experiments on SiO_2 particles impacting SiO_2 substrate, as shown in Fig. 6(g). The value of α is taken as 0.57 because the particle and target are same materials [44]. The Y of the SiO_2 is measured to be 1174±170 MPa [Fig. 6(h)].

The spectrum of the impact modes according to the φ is shown in Fig. 7, and the detailed data is listed in supplementary materials, Table S1. The calculated φ-values for the splatting mode ($\varphi << 1$) of the CoCrNi coating (red reflective dot in Fig. 7), for the penetration mode ($\varphi >> 1$) of the Al coating (green and purple reflective dots in Fig. 7), and for the co-deformation mode ($\varphi \approx 1$) of the Cu coating (carmine and black reflective dots in Fig. 7) are consistent with experimental results (Fig. 4). Moreover, the impact modes of the CoCrNi coating subjected to Al, Ni, Ti, Zn, Ag, Cu, Ti, Ni, and W microparticles are investigated, where the materials properties of these microparticles are given in supplementary materials, Table S2. Except for the W microparticle, all the other microparticles are in the splatting mode, showing that the CoCrNi coating is a superb impact-protection coating subjected to the majority of metallic microparticles. Although the W microparticle has the penetration mode for the CoCrNi coating, its φ-value is much smaller than the other materials subjected to the W microparticle impact, implying that the CoCrNi coating should have the least damage. Therefore, our study provides direct proof of the CoCrNi coating with extraordinary impact resistance subjected to microparticle impact and suggests promising engineering applications as protective coatings for equipment to enhance surface integrity and reliability subjected to high-speed collisions of solid particles such as ice and sand dust.

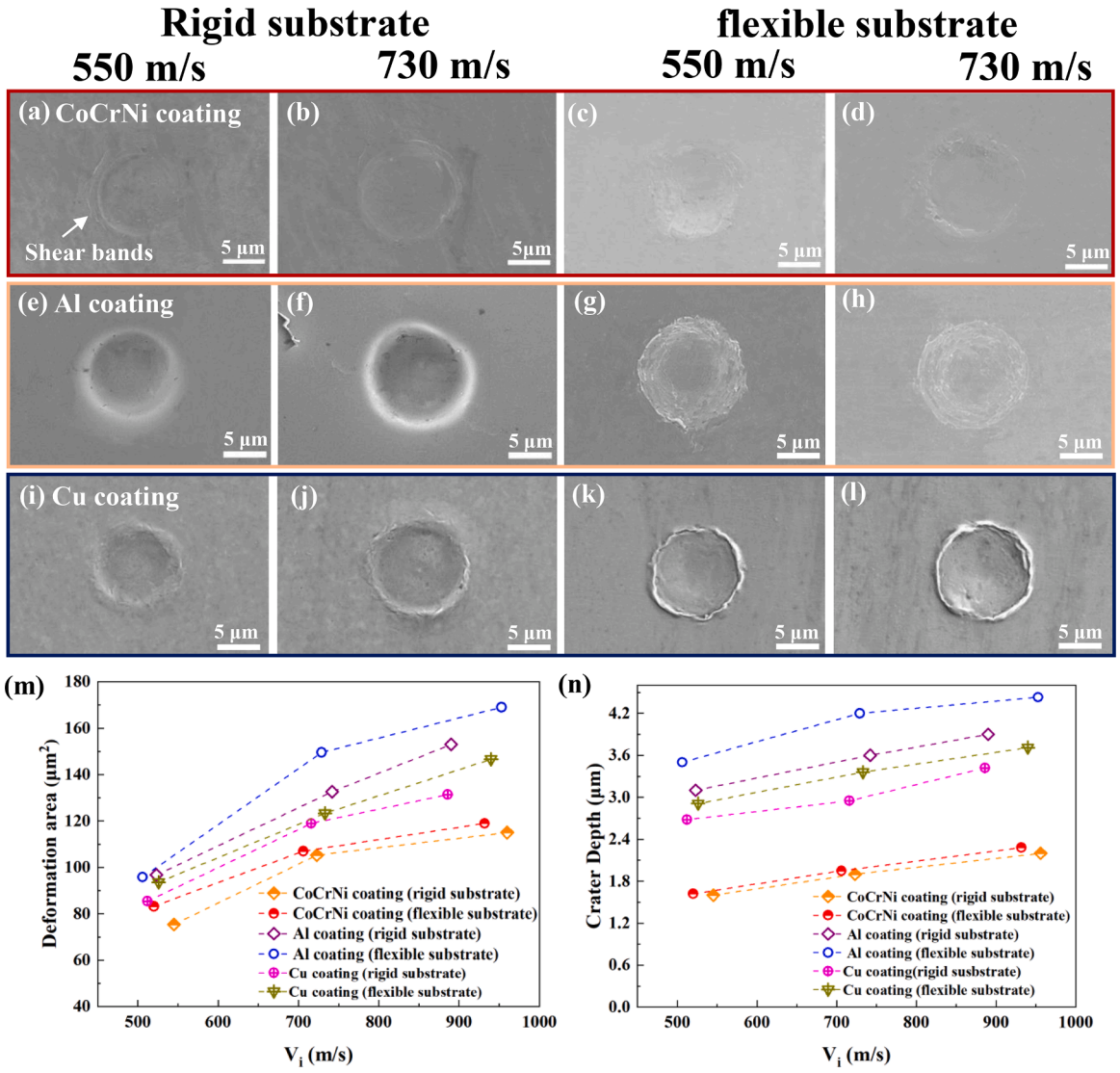

Fig. 4. (a–l) Post-impact observations of the CoCrNi, the Al, and the Cu coatings with rigid and flexible substrates at V_i of 550 and 730 m/s, respectively. (m) Deformation area and (n) crater depth of the CoCrNi, the Al, and the Cu coatings corresponding to different V_i.

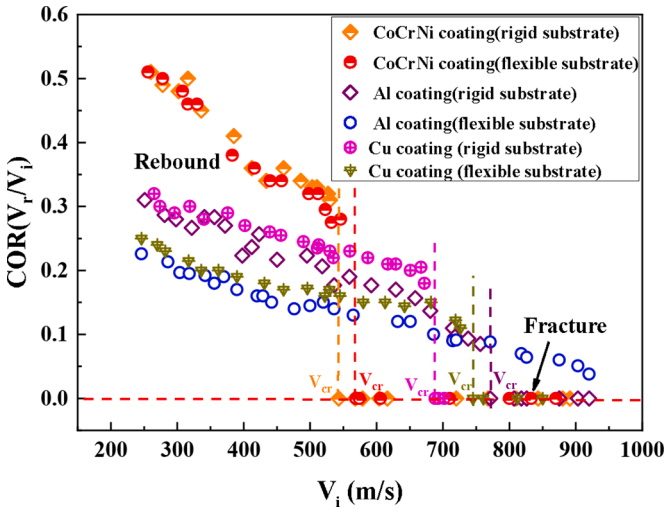

Fig. 5. COR for microparticle impacts on the CoCrNi, the Al, and the Cu coatings with rigid and flexible substrates.

4. Conclusions

In this paper, the CoCrNi MEA coating were fabricated, and its protective performance was investigated. The main conclusions are as follows.

1 The amorphous CoCrNi MEA coatings with a thickness of 4.5 μm were synthesized using IBAD on the rigid and flexible substrates. The CoCrNi coatings exhibited a high hardness of 9.7 GPa and an elastic modulus of 146.8 GPa under the nanoindentation test.
2 Regardless of the flexible or the rigid substrates, the CoCrNi coatings had a smaller deformation area and crater depth than the Al coatings. In addition, the crater depths of the CoCrNi coating were much smaller than its thickness, showing good protection for the substrates.
3 The CoCrNi coatings had a higher COR and a lower critical velocity than the Al and the Cu coating, indicating higher impact resistance of the CoCrNi coatings compared to the Al and the Cu coatings.
4 Most metallic particles were in the splatting mode when impacting the CoCrNi coatings except the W particles, indicating extraordinary impact resistance of the CoCrNi coatings subjected to microparticle

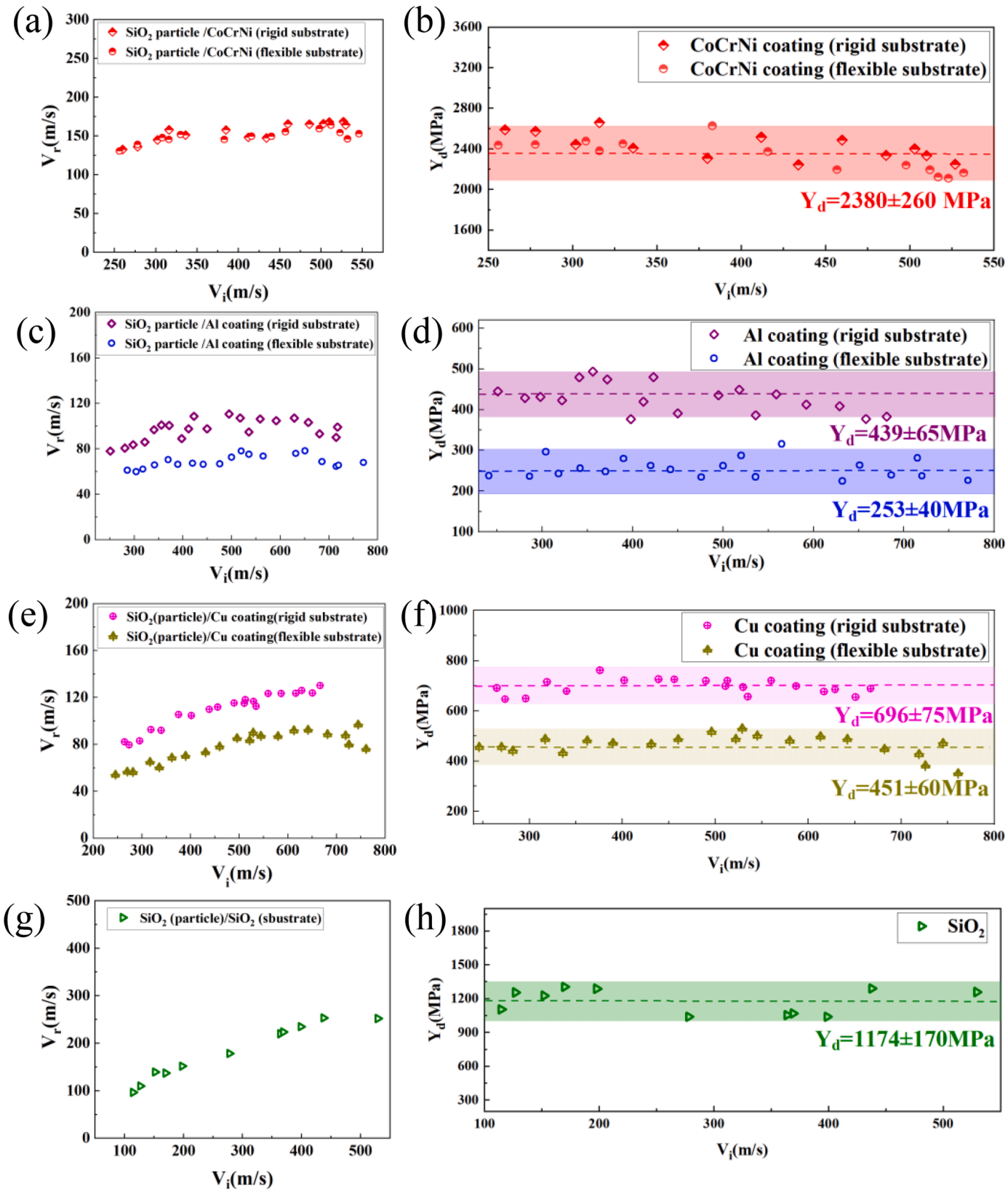

Fig. 6. The *Y* of the CoCrNi coating, the Al coating, the Cu coating, and SiO_2 measured by LIPIT experiments.

impact and suggesting promising engineering applications as protective coatings.

CRediT authorship contribution statement

J.L. Dong: Conceptualization, Data curation, Formal analysis, Investigation, Writing – original draft. **F.C. Li:** Resources, Formal

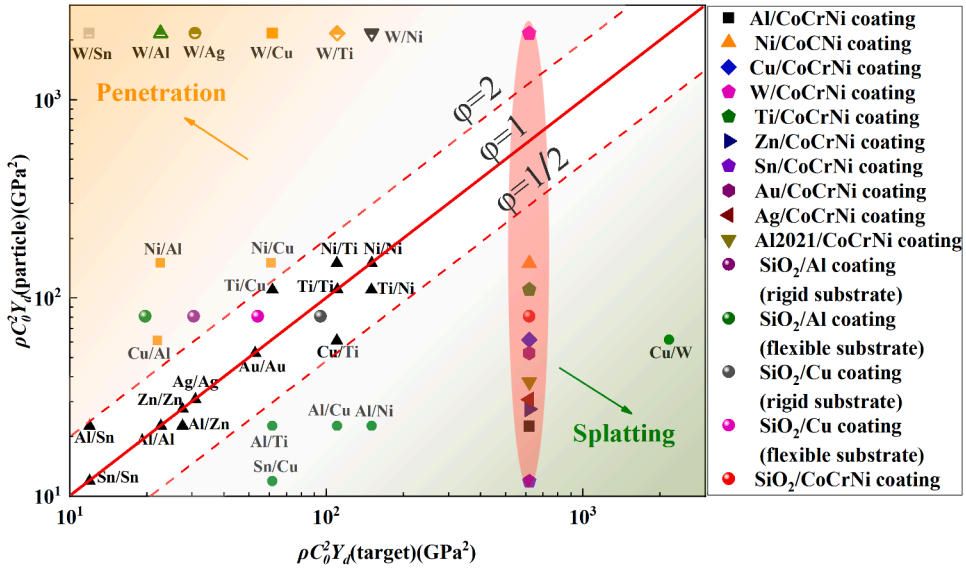

Fig. 7. Spectrum for impact modes of the CoCrNi coating subjected to various microparticle impacts. The diagonal line corresponds to $\varphi = 1$. The dotted lines correspond to $\varphi = 1/2$ and $\varphi = 2$. Data for Al on Al, Zn on Zn, Cu on Cu, Ni on Ni, Sn on Sn, Al on Zn, Al on Sn, Au on Au, Ag on Ag, Ti on Ti, Ni on Al, Ni on Cu, Ni on Ti, and Ti on Ni are from Ref [42].

analysis, Methodology. **X.Q. Wu:** Conceptualization, Methodology, Formal analysis, Writing – original draft, Writing – review & editing, Supervision, Funding acquisition. **G.J. Wang:** Conceptualization, Formal analysis, Writing – review & editing, Supervision, Funding acquisition. **X.P. Zhang:** Resources, Formal analysis. **B.Q. Luo:** Resources, Formal analysis. **X.M. Chen:** Resources, Formal analysis. **F.L. Tan:** Supervision. **Y.H. Liu:** Resources, Formal analysis, Supervision. **M. Q. Jiang:** Resources, Formal analysis, Supervision. **J.H. Zhao:** Supervision. **C.G. Huang:** Funding acquisition, Supervision. **C.W. Sun:** Supervision.

Declaration of Competing Interest

The authors declare that they have no known competing financial interests or personal relationships that could have appeared to influence the work reported in this paper.

Data availability

Data will be made available on request.

Acknowledgments

This work was supported by the National Key R&D Program of China (Grant No. 2021YFA0719200) and the National Natural Science Foundation of China (Grant Nos. 92166201 and 12232020).

Supplementary materials

Supplementary material associated with this article can be found, in the online version, at doi:10.1016/j.ijimpeng.2023.104714.

References

[1] George EP, Raabe D, Ritchie RO. High-entropy alloys. Nat Rev Mater 2019;4:515–34.
[2] Zhang W, Liaw PK, Zhang Y. Science and technology in high-entropy alloys. Science China Materials 2018;61:2–22.
[3] Yong Z, Zuo TT, Zhi T, Gao MC, Dahmen KA, Liaw PK, Zhao PL. Microstructures and properties of high-entropy alloys. Prog Mater Sci 2014;61:1–93.
[4] Ye YF, Wang Q, Lu J, Liu CT, Yang Y. High-entropy alloy: challenges and prospects. Mater Today 2016.
[5] Yeh JW, Chen YL, Lin SJ, Chen SK. High-Entropy Alloys – A New Era of Exploitation. Mater Sci Forum 2007:1–9.
[6] Bernd G, Anton H, Dhiraj C, Chang EH, George EP, Ritchie RO. A fracture-resistant high-entropy alloy for cryogenic applications. Science 2014;345:1153.
[7] Gludovatz B, Hohenwarter A, Thurston KVS, Bei H, Wu Z, George EP, Ritchie RO. Exceptional damage-tolerance of a mediumentropy alloy CrCoNi at cryogenic temperatures. Nat Commun 2016;7:1–8.
[8] Yang M, Zhou L, Wang C, Jiang P, Wu X. High impact toughness of CrCoNi medium-entropy alloy at liquid-helium temperature. Scr Mater 2019;172:66–71.
[9] Li Z, Pradeep KG, Deng Y, Raabe D, Tasan CC. Metastable high-entropy dual-phase alloys overcome the strength–ductility trade-off. Nature 2016;534:227–30.
[10] Ren J, Zhang Y, Zhao D, Chen Y, Guan S, Liu Y, Liu L, Peng S, Kong F, Poplawsky JD. Strong yet ductile nanolamellar high-entropy alloys by additive manufacturing. Nature 2022;608:62–8.
[11] Zhang TW, Ma SG, Zhao D, Wu YC, Zhang Y, Wang ZH, Qiao JW. Simultaneous enhancement of strength and ductility in a NiCoCrFe high-entropy alloy upon dynamic tension: micromechanism and constitutive modeling. Int J Plast 2020;124:226–46.
[12] Li Z, Tasan CC, Pradeep KG, Raabe D. A TRIP-assisted dual-phase high-entropy alloy: grain size and phase fraction effects on deformation behavior. Acta Mater 2017;131:323–35.
[13] Liu XF, Tian Z, Zhang XF, Chen HH, Dai LH. Self-sharpening" tungsten high-entropy alloy. Acta Mater 2020;186:257–66.
[14] Lu C, Niu L, Chen N, Jin K, Yang T, Xiu P, Zhang Y, Gao F, Bei H, Shi S, He MR, Robertson IM, Weber WJ, Wang L. Enhancing radiation tolerance by controlling defect mobility and migration pathways in multicomponent single-phase alloys. Nat Commun 2016;7:13564.
[15] Juan C, Tsai M, Tsai C, Lin C, Wang W, Yang C, Teh J-W. Enhanced mechanical properties of HfMoTaTiZr and HfMoNbTaTiZr refractory high-entropy alloys. Intermetallics 2015;62:76–83.
[16] Dada M, Popoola P, Adeosun S, Mathe N. High entropy alloys for aerospace applications. Environ Impact Aviation Sustain Sol [Working Title] 2019.
[17] Jian YA, Ke SA, Wei ZA, Qc A, Zn B, Cz A, Jl A, Yy A, Ning LA, Wei ZC. A novel AlCrFeMoTi high-entropy alloy coating with a high corrosion-resistance in lead-bismuth eutectic alloy. Corros Sci 2021.
[18] Deng J, Yang J, Lv L, Zhang W, Chen Q, Zhou M, Zhu C, Liu N, Yang J. Corrosion behavior of refractory TiNbZrMoV high-entropy alloy coating in static lead-bismuth eutectic alloy: a novel design strategy of LBE corrosion-resistant coating. Surf Coat Technol 2022:448.
[19] Cheng J, Sun B, Ge Y, Hu X, Zhang L, Liang X, Zhang X. Nb doping in laser-cladded Fe25Co25Ni25(B0.7Si0.3)25 high entropy alloy coatings: microstructure evolution and wear behavior. Surf Coat Technol 2020;402. 126321-.
[20] Cao F, Munroe P, Zhou Z, Xie Z. Medium entropy alloy CoCrNi coatings: enhancing hardness and damage-tolerance through a nanotwinned structuring. Surf Coat Technol 2018;335:257–64.
[21] Carter TJ. Common failures in gas turbine blades. Eng. Fail. Anal. 2005;12:237–47.
[22] Chen S, Gad E, Zhang L, Lam N, Xu S, Lu G. Experiments on an ice ball impacting onto a rigid target. Int J Impact Eng 2022:167.
[23] Tang Y, Li DY. Dynamic response of high-entropy alloys to ballistic impact. Sci Adv 2022;8:1–8.

[24] Tfc A, Phc A, Clt A, Yll A, Lmw B, Cyc C, Jwy D, Cnh E, Dzo F, Jry A. Investigation on the ballistic induced nanotwinning in the Mn-free Fe 27 Co 24 Ni 23 Cr 26 high entropy alloy plate. Mater Chem Phys 2021.
[25] Shi Kaiwei, Cheng Junchao, Cui Lang, Qiao Junwei, Huang Junyu, Zhang Min, Yang Huijun, Wang Z. Ballistic impact response of Fe40Mn20Cr20Ni20 high-entropy alloys. J Appl Phys 2022:132.
[26] Greer JR, Hosson J. Plasticity in small-sized metallic systems: intrinsic versus extrinsic size effect. Prog Mater Sci 2011;56:654–724.
[27] Zhang Q, Huang R, Jiang J, Cao T, Zeng Y, Li J, Xue Y, Li X. Size effects and plastic deformation mechanisms in single-crystalline CoCrFeNi micro/nanopillars. J Mech Phys Solids 2022:162.
[28] Zhang Q, Huang R, Zhang X, Cao T, Xue Y, Li X. Deformation mechanisms and remarkable strain hardening in single-crystalline high-entropy-alloy micropillars/nanopillars. Nano Lett 2021;21:3671–9.
[29] Gali A, George EP. Tensile properties of high- and medium-entropy alloys. Intermetallics 2013;39:74–8.
[30] Laplanche G, Kostka A, Reinhart C, Hunfeld J, Eggeler G, George EP. Reasons for the superior mechanical properties of medium-entropy CrCoNi compared to high-entropy CrMnFeCoNi. Acta Mater 2017;128:292–303.
[31] D. Veysset, J.H. Lee, M. Hassani, S.E. Kooi, K.A. Nelson, High-velocity micro-projectile impact testing: a review, (2020).
[32] Dong JL, Song X, Wang ZJ, Xiao KL, Jiang MQ. Impact resistance of single-layer metallic glass nanofilms to high-velocity micro-particle penetration. Extreme Mech Lett 2021:101258.
[33] Xu Y, Li G, Xia Y. Synthesis and characterization of super-hard AlCrTiVZr high-entropy alloy nitride films deposited by HiPIMS. Appl Surf Sci 2020:523.
[34] Musil J, Vlcek J. Magnetron sputtering of alloy and alloy-based films. Thin Solid Films 1999;343-344:47–50.
[35] Tsai CW, Lai SW, Cheng KH, H M. Strong amorphization of high-entropy AlBCrSiTi nitride film. Thin Solid Films 2012.
[36] Wang Z, Wang C, Zhao Y-L, Hsu Y-C, Li C-L, Kai J-J, Liu C-T, Hsueh C-H. High hardness and fatigue resistance of CoCrFeMnNi high entropy alloy films with ultrahigh-density nanotwins. Int J Plast 2020:131.
[37] Feng XB, Fu W, Zhang JY, Zhao JT, Li J, Wu K, Liu G, Sun J. Effects of nanotwins on the mechanical properties of Al x CoCrFeNi high entropy alloy thin films. Scr Mater 2017;139:71–6.
[38] Lee JH, Loya PE, Lou J, Thomas EL. Dynamic mechanical behavior of multilayer graphene via supersonic projectile penetration. Science 2014;346:1092.
[39] Hassani-Gangaraj M, Veysset D, Nelson KA, Schuh CA. Melting Can Hinder Impact-Induced Adhesion. Phys. Rev. Lett. 2017;119:175701.
[40] Schuh CA, Hufnagel TC, Ramamurty U. Mechanical behavior of amorphous alloys. Acta Mater 2007;55:4067–109.
[41] Greer AL, Cheng YQ, Ma E. Shear bands in metallic glasses. Mater. Sci. Eng. R 2013;74:71–132.
[42] Hassani M, Veysset D, Sun Y, Nelson KA, Schuh CA. Microparticle Impact-Bonding Modes for Mismatched Metals: from Co-Deformation to Splatting and Penetration. Acta Mater 2020.
[43] Wu CY, Li LY, Thornton C. Rebound behaviour of spheres for plastic impacts. Int J Impact Eng 2003;28:929–46.
[44] Sun Y, Veysset D, Nelson KA, Schuh CA. The transition from rebound to bonding in high-velocity metallic microparticle impacts: jetting-associated power-law divergence. J Appl Mech 2020;87:1–28.